Prc1E and Kif4A control microtubule organization within and between large *Xenopus* egg asters

P. A. Nguyen, C. M. Field, and T. J. Mitchison*
Department of Systems Biology, Harvard Medical School, Boston, MA 02115; Marine Biological Laboratory, Woods Hole, MA 02543

ABSTRACT **The cleavage furrow in *Xenopus* zygotes is positioned by two large microtubule asters that grow out from the poles of the first mitotic spindle. Where these asters meet at the midplane, they assemble a disk-shaped interaction zone consisting of anti-parallel microtubule bundles coated with chromosome passenger complex (CPC) and centralspindlin that instructs the cleavage furrow. Here we investigate the mechanism that keeps the two asters separate and forms a distinct boundary between them, focusing on the conserved cytokinesis midzone proteins Prc1 and Kif4A. Prc1E, the egg orthologue of Prc1, and Kif4A were recruited to anti-parallel bundles at interaction zones between asters in *Xenopus* egg extracts. Prc1E was required for Kif4A recruitment but not vice versa. Microtubule plus-end growth slowed and terminated preferentially within interaction zones, resulting in a block to interpenetration that depended on both Prc1E and Kif4A. Unexpectedly, Prc1E and Kif4A were also required for radial order of large asters growing in isolation, apparently to compensate for the direction-randomizing influence of nucleation away from centrosomes. We propose that Prc1E and Kif4, together with catastrophe factors, promote "anti-parallel pruning" that enforces radial organization within asters and generates boundaries to microtubule growth between asters.**

Monitoring Editor
Thomas Surrey
The Francis Crick Institute

Received: Sep 5, 2017
Revised: Nov 13, 2017
Accepted: Nov 22, 2017

INTRODUCTION

Symmetric cell division requires precise positioning of the cleavage furrow at the midplane of a cell. During anaphase, animal somatic cells assemble a bipolar microtubule array in the cell center called the cytokinesis midzone or central spindle (Glotzer, 2009). Midzone microtubules are orientated with plus ends toward the midplane and a small antiparallel overlap at the equator (McIntosh and Euteneuer, 1984; Mastronarde *et al.*, 1993). The plus-end–directed kinesin-family motor Kif23 (a.k.a. MKLP1) transports the furrow-stimulating factor RacGap1 (together they constitute the centralspindlin complex) to the center of the midzone (Mishima *et al.*, 2002), while the plus-end–directed motor Kif20A (a.k.a. MKLP2) transports the chromosome passenger complex (CPC) (Gruneberg *et al.*, 2004). Centralspindlin and the CPC then signal locally to the equatorial cortex to initiate the furrow (Jantsch-Plunger *et al.*, 2000; Yüce *et al.*, 2005; Canman *et al.*, 2008; Lewellyn *et al.*, 2011; Argiros *et al.*, 2012; Basant *et al.*, 2015; Henson *et al* 2016). In addition, astral microtubules and/or kinetochores may relax the cortex and inhibit furrow formation at the poles in some systems (White and Borisy, 1983; Rodrigues *et al.*, 2015). In cells forced to undergo monopolar cytokinesis, monopolar midzones assemble with microtubule plus ends oriented toward the side of the cell proximal to chromatin. Centralspindlin and CPC accumulate on that side, where they trigger highly asymmetric and incomplete cleavage (Canman *et al.*, 2003; Hu *et al.*, 2008; Shrestha *et al.*, 2012).

An important question in cytokinesis mechanism is how midzone microtubules, or their equivalents in large embryo cells, are spatially organized. The conserved cytokinesis proteins Prc1 and Kif4A play important roles in promoting anti-parallel organization at the midplane and determining midzone microtubule length (Kurasawa *et al.*, 2004; Hu *et al.*, 2011; Subramanian *et al.*, 2013). Their functions

This article was published online ahead of print in MBoC in Press (http://www.molbiolcell.org/cgi/doi/10.1091/mbc.E17-09-0540) on November 29, 2017.

*Address correspondence to: T. J. Mitchison (timothy_mitchison@hms.harvard.edu).

Abbreviations used: BSA, bovine serum albumin; CPC, chromosome passenger complex; CSF, cytostatic factor; EGTA, ethylene glycol-bis-(β-aminoethyl ether)-*N,N,N′,N′*-tetraacetic acid; GFP, green fluorescent protein; IgG, immunoglobulin G; KS, Kolmogorov–Smirnov; NCBI, National Center for Biotechnology Information; PEG, poly(ethylene glycol); PLL, poly(L-lysine); ROI, region of interest; TIRF, total internal reflection fluorescence.

have been extensively studied in somatic cells, and using pure proteins, but not in very large egg cells. Prc1 (a member of the Ase1/MAP65 family of microtubule cross-linkers) promotes anti-parallel bundling in the midzone (Jiang *et al.*, 1998; Mollinari *et al.*, 2002; Subramanian *et al.*, 2010). Prc1 can also organize parallel microtubule bundles in dividing cells. In cells undergoing monopolar cytokinesis, Prc1 is required to polarize the midzone and trigger furrowing (Shrestha *et al.*, 2012), and during normal division it transiently "tags" parallel bundles at plus ends (Subramanian *et al* 2013). Kif4A (a member of the Kinesin-4 family of plus-end–directed motors with plus-end polymerization-inhibiting activity) antagonizes growth of midzone plus ends (Bringmann *et al.*, 2004; Hu *et al.*, 2011). Prc1 and Kif4A interact dynamically during cytokinesis but do not form a stable complex (Zhu and Jiang, 2005). Together, they can generate anti-parallel overlaps of defined length in a pure protein system (Bieling *et al.*, 2010) and also "tag," and halt growth, of parallel bundles at plus ends (Subramanian *et al* 2013).

The large size of frog eggs make them an interesting system to study aster organization and cytokinesis signaling. The first mitotic spindle is small compared with the egg. At anaphase onset, large microtubule asters grow out from centrosomes at the spindle poles and expand toward the cortex, taking ~15 min to reach it in frog zygotes (Mitchison *et al.*, 2012). As the asters grow, the centrosomes and nuclei at their centers are pulled away from the midplane of the cell by dynein (Wühr *et al.*, 2010). In a *Xenopus* zygote fixed between first anaphase and first cytokinesis, microtubules from the two asters overlap and interact, forming a disk of antiparallel bundles at the midplane. This disk, which we will call the aster interaction zone, recruits CPC and centralspindlin. It expands outward toward the cortex as the asters enlarge and initiates a furrow where, and when, it touches the cortex (Nguyen *et al.*, 2014; Field *et al.*, 2015). The interaction zone between asters is functionally equivalent to the midzone in a dividing somatic cell, but it extends out much further from the position previously occupied by the metaphase plate.

The interaction zone between asters in frog eggs appears to limit microtubule growth and prevent interpenetration of the two asters, as evidenced by lower microtubule density in the zone compared with nearby regions (Mitchison *et al.*, 2012). Using EB1 tracking in an extract system, we directly observed that microtubules from one aster tend to stop at the interaction zone and do not cross between asters (Nguyen *et al.*, 2014). This block to microtubule interpenetration between asters is presumably important for correct CPC and centralspindlin localization. It may also serve to generate microtubule length asymmetries that promote dynein-mediated movement of centrosomes away from the midplane (Wühr *et al.*, 2010). Based on prior work in somatic cells and with pure proteins (cited above), Prc1 and Kif4A are candidates for mediating the block to microtubule growth between asters. Prc1 has been little characterized in *Xenopus* eggs, where it is present as the egg-specific homologue Prc1E (Nguyen *et al* 2014). *Xenopus* Kif4A (previously called Xklp1) was shown to be expressed in eggs and essential for normal cleavage (Vernos *et al.*, 1995). That paper focused on Kif4A localization to mitotic chromosomes and led to the concept of "chromokinesins."

Here we use the *Xenopus egg* extract system to probe the role of Prc1 and Kif4A in controlling microtubule dynamics within, and between, large interphase asters. In Nguyen *et al.* (2014) we reported that Prc1E and Kif4A are recruited to anti-parallel bundles between asters and that Kif4A is required for normal microtubule organization and CPC transport. We did not investigate the effect of Prc1E depletion on Kif4A localization or vice versa, and we did not investigate the effect of either depletion on EB1 comet dynamics. These experiments are reported below. In the course of this analysis, we made an unexpected finding: that Prc1E and Kif4A work together to enforce radial order in expanding single asters, presumably by recognition and pruning of accidental anti-parallel overlaps. Our findings extend understanding of the cell division biology of the conserved Prc1/Kif4A module and reveal interesting adaptations to promote microtubule organization and cleavage in very large egg cells.

RESULTS

Prc1E and Kif4A expression in *Xenopus* zygotes

We first identified the egg forms of Prc1 and Kif4A and generated antibodies to localize them in zygotes and deplete them in extracts. NCBI identifiers for each protein are listed in Supplemental Table S1. By proteomic analysis, *Xenopus* eggs express do not express detectable levels of somatic Prc1 (inferred from proteomics in Wühr *et al.* (2014). We confirmed this by Western blot with an anti-peptide antibody (not shown). Instead, eggs express a Prc1 isoform, called "Protein Regulator of Cytokinesis-Like (PRC1L)" in NCBI databases, that we will call Prc1E to reflect its egg specific expression. Prc1E is ~45% identical to Prc1 and is present in eggs at ~60 nM (inferred from proteomics in Wühr *et al.*, 2014). Prc1E is gradually replaced by somatic Prc1 during development (inferred from mRNA and proteome analysis in Peshkin *et al.*, 2015). Somatic Kif4A is present at ~100 nM in eggs, and there is no evidence for egg-specific isoforms by proteomics (Wühr *et al.*, 2014). We raised affinity-purified rabbit antibodies to a C-terminal peptide from Prc1E and to the entire nonmotor region of Kif4A. These antibodies were described and characterized previously using standard methods (Nguyen *et al.*, 2014; Mitchison *et al.*, 2013). For this study, we performed immunoprecipitation-mass spectrometry analysis, from which we concluded that our antibodies recognize native protein and are specific for their primary target over all cell division proteins and that Prc1E and Kif4A do not coimmunoprecipitate, suggesting they do not form a stable complex in solution.

Having identified Prc1E and Kif4A as the form of this conserved cytokinesis module that is expressed in eggs, we probed their localization in fixed zygotes. We focused on the period between first mitosis and first cleavage, when a pair of asters grows out from the poles of the mitotic spindle to position the furrow. The boundary region between asters excluded our Prc1E antibody (not shown), even though this protein localizes to anti-parallel microtubule bundles in extract (see below). We suspect this negative result on localization in fixed zygotes was an artefact caused by lack of antibody penetration, which is known for somatic midzone staining (Saxton and McIntosh, 1987) or by failure of our antibody to recognize a phosphorylated form of Prc1E. Kif4A was enriched on anti-parallel bundles between asters, where it mostly colocalized with the AurkB subunit of the CPC (Figure 1). The CPC sometimes appeared to be more focused at the center of antiparallel bundles than Kif4A (Figure 1, A and C). Weak Kif4A staining was observed throughout asters, suggesting that Kif4A does not require anti-parallel bundles for recruitment to microtubules. Kif4A was also present on mitotic chromosomes shortly after anaphase onset, consistent with its function as a chromokinesin (Figure 1A).

Prc1E and Kif4A localization in interphase egg extracts

To more reliably localize Prc1E and Kif4A, and probe their dynamics and function, we turned to an actin-intact egg extract system that reconstitutes spatially organized cytokinesis signalling (Field *et al.*, 2014). We used magnetic beads coated with anti-Aurora A kinase

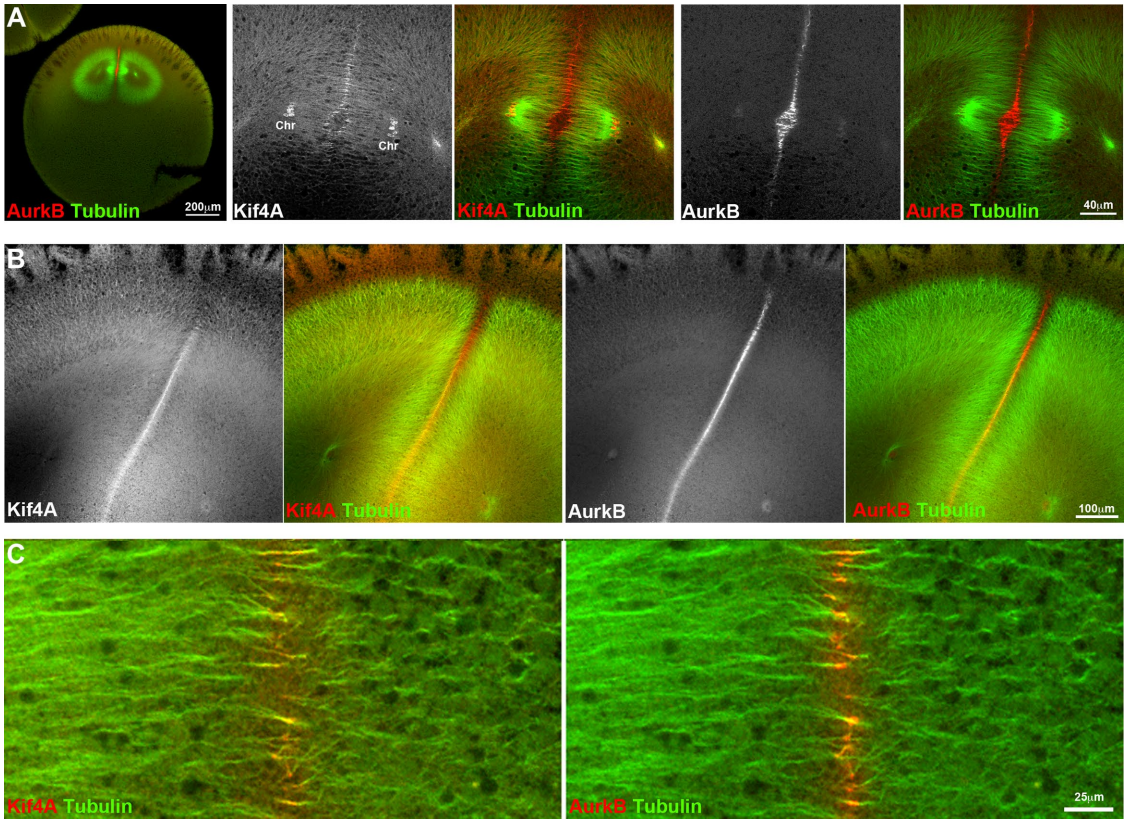

FIGURE 1: Kif4A localization at aster interaction zones in zygotes. *Xenopus* eggs were fixed between first mitosis and first cleavage (70–100 min postfertilization), triple stained for Kif4A, AurkB (a subunit of the CPC), and tubulin, and imaged by laser scanning confocal microscopy in a clearing solvent. (A) Anaphase–telophase. Kif4A is enriched at anti-parallel bundles between asters. At this stage, it is still present on mitotic chromosomes (Chr). (B) Shortly before the asters reach the cortex. Kif4A is enriched at the interaction zone between asters, where it colocalizes with the CPC. (C) Similar stage to B, different embryo. Higher magnification of the interaction zone between asters illustrating anti-parallel microtubule bundles with Kif4A and CPC enriched at the midline.

(AurkA) immunoglobulin G (IgG) as model centrosomes (Tsai and Zheng, 2005). Prc1E and Kif4A were visualized by addition of green and red fluorescent recombinant fusion proteins whose biochemical characterization is shown in Supplemental Figure 1A. Later depletion–add back experiments (Figure 5) showed they were functionally competent. For visualization experiments, we added these to extract at <20% of the concentration of endogenous proteins to minimize perturbation. We reported previously that Prc1E and Kif4A are enriched in anti-parallel bundles between asters in the extract system (Nguyen *et al.*, 2014). Here we report dynamics and more careful analysis using kymographs.

Both Prc1E and Kif4A were recruited to microtubules and localized throughout asters. When the asters grew into each other, Prc1E became weakly enriched, and Kif4A strongly enriched, on anti-parallel bundles between the asters (Figure 2a, 19 and 23 min, and Supplemental Video 1). The two proteins colocalized on some bundles, but their overall distribution differed, consistent in their interacting transiently on microtubules but not forming a stable complex in solution (Zhu and Jiang, 2005; Bieling *et al.*, 2010). To quantify microtubule morphology and Prc1E/Kif4A recruitment over time, we generated kymograph plots along the line connecting the two aster centers, shown in the blue rectangle (Figure 2a′). These plots confirmed Prc1E and Kif4A recruitment to anti-parallel bundles between the asters. Both were recruited at the same time, and Kif4A was always more enriched in the interaction zone. We also observed bright streaks of Prc1E and Kif4A at the free edges of growing asters (Figure 2a, zoom-ups within yellow square). These probably correspond to Prc1/Kif4A positive "plus end tags" observed in dividing somatic cells (Subramanian *et al.*, 2013) that result from Kif4A transport to plus ends, followed by stabilization of plus ends by the two proteins. We also coimaged the CPC with Prc1E and tubulin, adding a GFP-tagged DasraA subunit of the CPC for visualization (Figure 2b and Supplemental Video 2). Unlike Prc1E and Kif4A, the CPC localized exclusively to a narrow region at the interaction zone and was not present in streaks elsewhere in asters. The tight localization at interaction zones was quantified using kymograph plots within the blue rectangle (Figure 2b′).

Plus-end dynamics at interaction zones between asters

To provide a quantitative assay for the block to microtubule growth between asters, we imaged growing plus ends between two asters with EB1-GFP and tracked them using PlusTipTracker software (Applegate *et al.*, 2011). Figure 3a and Supplemental Video 3 show EB1 trajectories color-coded by the orientation of microtubule growth. Quantification of EB1 growth direction (Figure 3e) showed that more than 90% of the growing microtubules within each aster were oriented with their plus ends pointing radially away from the nucleating site, and orientation switched abruptly over ~40 μm at the boundary between asters. Similar directionality data were reported previously using total internal reflection fluorescence (TIRF)

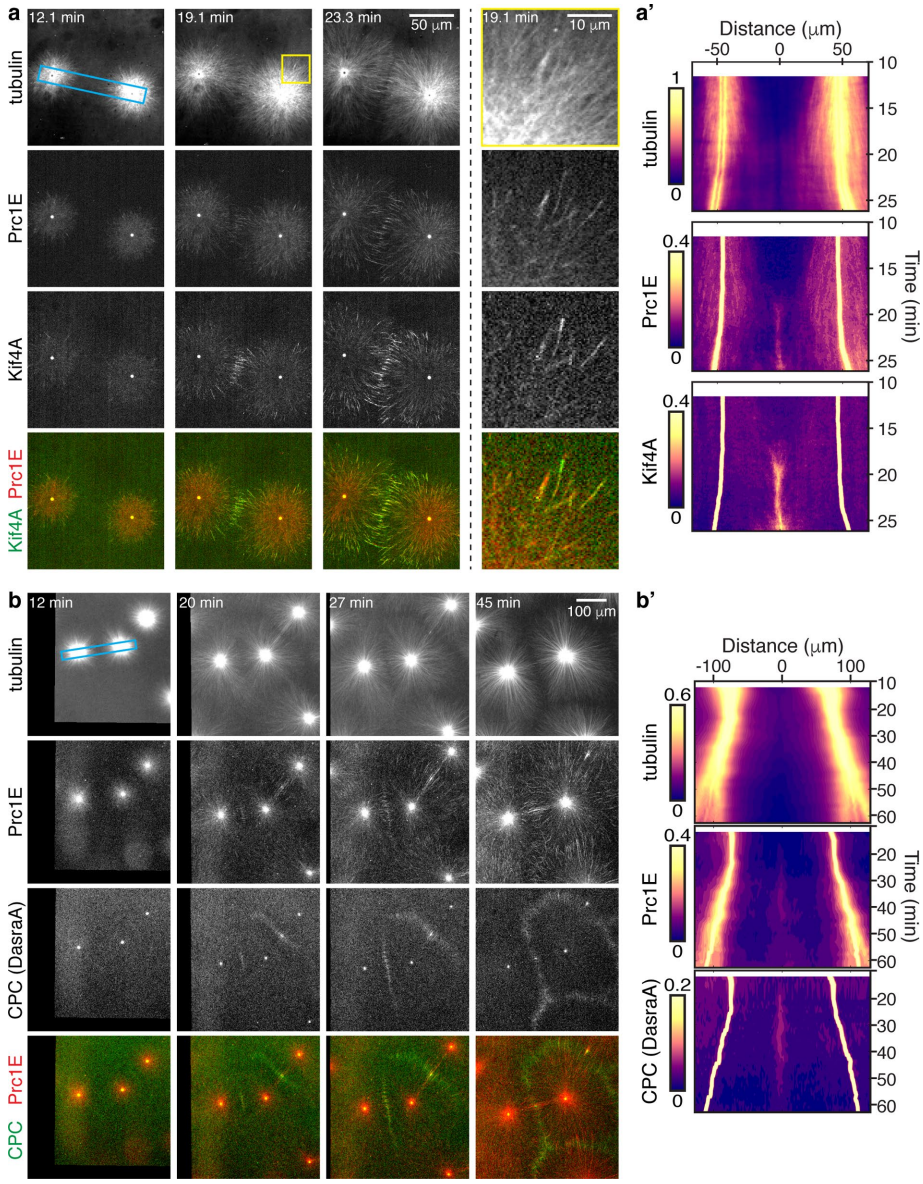

FIGURE 2: Localization of Prc1E and Kif4A in interphase egg extracts. (a) Spinning disk confocal time-lapse sequence of asters nucleated from AurkA beads in interphase extract. Probes: microtubules (Alexa 647-tubulin), mCherry-Prc1E, and Kif4A-GFP (Supplemental Video 1). (b) Widefield sequence using GFP-DasraA subunit to visualize the CPC (Supplemental Video 2). (a', b') Kymograph analysis along a 30-μm-wide line (cyan box in a and b). Note that the CPC is more focused in interaction zones than Prc1E or Kif4A.

imaging (Nguyen *et al.*, 2014). We next mapped EB1 comet velocities (Figure 3, b and f), initiations (Figure 3, b and h), terminations (Figure 3, c and h), and density (Figure 3g). EB1 comets tended to slow down as they entered the interaction zone, as evidenced by enrichment of blue colors at the midline in Figure 3b and the central dip in Figure 3f. Mean growth rates in one experiment were 25.8 ± 9.9 μm/min (± SD, n = 13,632 comets) outside the interaction zone and 22.9 ± 1 1.0 μm/min (± SD, n = 3172 comets) inside it, representing an 11% reduction (the two rate distributions were statistically significantly different, $p < 10^{-45}$ from Kolmogorov–Smirnov [KS] test). Full biological repeat experiments showed qualitatively similar slowdowns (11.3 ± 2.3% reduction, mean ± SD, n = 5 interaction zones, $p < 0.001$ from one-sample t test; also see Figure 3h). EB1 track initiations, which correspond to nucleation and/or rescue events, were uniformly distributed (Figure 3, c and h). Termination events, which correspond to catastrophes or pauses, were enriched at the center of the interaction zone (Figure 3, d and h). Comet density was lower near the aster centers but not specifically increased in the interaction zone (Figure 3g). From analysis of multiple representative zones, we observed no strong spatial regulation of either EB1 comet density (10 ± 39% reduction, mean ± SD from n = 5 interaction zones, p = 0.59 from one-sample t test) or of the spatial frequency of initiation events (15 ± 33% increase, p = 0.37). However, we saw a consistent increase in the frequency of termination events in or near the interaction zone midline (86 ± 33% increase, p = 0.004). Thus, plus ends tended to slow down and terminate more within interaction zones than elsewhere in asters, but the density of growing plus ends and the frequency of nucleation/rescue (which are hard to distinguish by EB1 tracking) are not spatially regulated. Spatially uniform nucleation of plus ends throughout large asters was quantified previously and shown to drive aster growth by mathematical modelling (Ishihara *et al.*, 2014, 2016).

A limitation of EB1 tracking is that it does not report on catastrophes or depolymerization. To gain longer-time-scale information on dynamics at boundaries between asters, we imaged labeled tubulin for a prolonged time interval, using a lower magnification to minimize photobleaching and focal plane drift. We found that once asters grew into contact, the total microtubule density at boundaries remained approximately constant for 40 min (Figure 3i). We were not able to quantify microtubule density from tubulin images, but these long-time-scale data rule out a continuous buildup of anti-parallel bundles microtubules over time. This approximate steady state in total microtubule density implies that all plus-end polymerization reported by the EB1 probe must be balanced by an equal amount of depolymerization, most likely by catastrophe at plus ends. We previously estimated that individual microtubules inside interphase asters in the extract system undergo catastrophes at a rate of ~3 min^{-1} (Ishihara *et al* 2016). Since the rates of EB1 comet initiation and termination are not very different in the boundary region between asters compared with the bulk aster (Figure 3h), and both regions are approximately at steady state in microtubule density (Figure 3i), we estimate that the catastrophe rate in anti-parallel bundles must be of similar order, that is, >1 min^{-1}. Thus, we infer that inhibition of plus-end growth in anti-parallel bundles must be followed by catastrophe. Alternatively, it is possible that anti-parallel bundles form early and then do not turn over or recruit new microtubules, but this seems unlikely given that EB1 comets appear to track into anti-parallel bundles continuously.

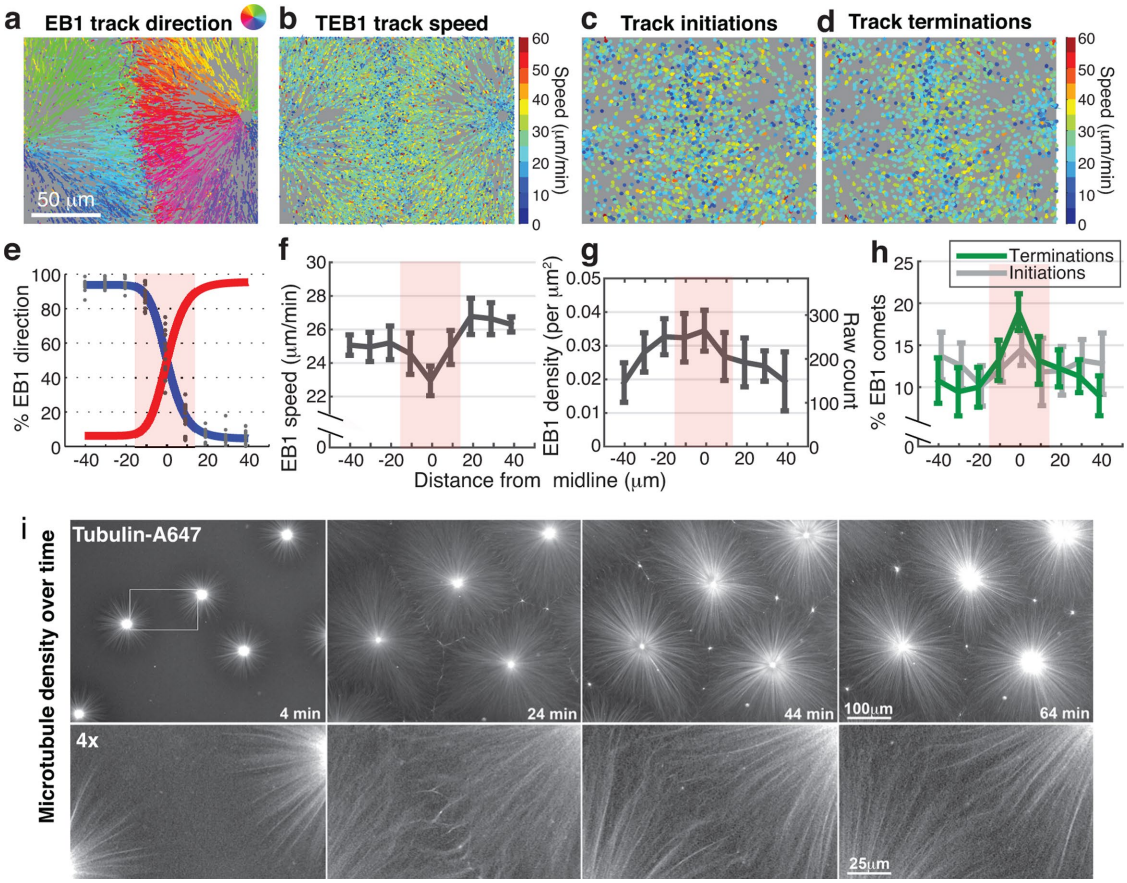

FIGURE 3: Visualization of microtubule dynamics between asters. Panels a–h show analysis of EB1-GFP trajectories imaged by spinning disk confocal microscopy at interaction zones between two asters. (a) EB1 comet trajectories colored by mean direction. (b) EB1 comet trajectories colored by instantaneous velocity. (c) EB1 comet initiations colored by velocity for 5 s after initiation. (d) EB1 comet termination colored by velocity 5 s before termination. (e) Spatial distributions EB1 comet trajectories classified by direction (gray dots: fraction of EB1 comets moving from left to right; blue curve: sigmoidal fit to grey dots; red curve: sigmoidal fit to fraction of EB1 comets moving in opposite direction). (f) Mean instantaneous growth rates (mean ± SEM). (g) EB1 comet density. (h) Fractions of EB1 comets that are growth initiation/terminations (mean ± SD), $n = 12$ neighboring ROIs (see *Materials and Methods* for data analysis). (i) Tubulin-A647 image sequence of a field of asters growing and interacting; 20× widefield. Interaction zones between asters were established by 24 min in this example. Note that the microtubule density between asters remained approximately constant for a further 40 min, showing that there is no increase in the density of anti-parallel bundles over time. Images were linearly rescaled to 8 bits to correct for mild photobleaching over the long image sequence.

Kif4A requires Prc1E for localization to anti-parallel bundles

To test the function of Prc1E and Kif4A in aster organization, we depleted each protein to less than 5% of its initial abundance. We depleted Kif4A previously in Nguyen *et al.* (2014) and noted strong disorganization of anti-parallel bundles between asters, and also defects in focusing the CPC at the center of the aster interaction zone. We did not deplete Prc1E or test the effect of Kif4A depletion on Prc1E localization or on EB1 comets trajectories. Figure 4 shows an overview of depletion effects and Figure 5 a detailed analysis of microtubule dynamics. Western blots quantification of depletions and add-backs are shown in Supplemental Figure 1, b–e, which is directly associated with Figure 5. Mass spectrometry analysis of these immunopreciptates showed that Prc1E and Kif4A did not significantly coimmunoprecipitate (data not shown), so we could measure the effect of depletions independently.

Figure 4a shows an overview of the effects of depleting Prc1E or Kif4 or inhibiting the AurkB subunit of the CPC with the small molecule ZM447439. We observed no obvious effect on nucleation from AurkA beads or on microtubule polymerization rates (measured by EB1 tracking) for any of these perturbations. Formation of regions of low microtubule density between asters were inhibited by all three perturbations, suggesting that Prc1E, Kif4, and CPC activity are all required for formation of sharp boundaries between asters.

We next probed dependency relationships for localization to bundles using fluorescently labeled proteins. Kif4A no longer localized to bundles when Prc1E was depleted (Figure 4c). Prc1E still localized when Kif4A was depleted, though the bundles were longer and more disorganized (Figure 4d). Inhibition of AurkB caused profound randomization of bundle position relative to the midline between the asters, but Prc1E and Kif4A still localized to bundles and to some extent still co-localized (Figure 4e). These data suggest a model where Prc1E recognizes anti-parallel bundles and then recruits Kif4A, consistent with the model previously developed using pure proteins (Bieling *et al.*, 2010). AurkB activity was not required for recruitment of either protein to bundles. However, AurkB activity was required for focusing Prc1E/Kif4A-positive bundles into a sharp line that bisects the distance between the asters.

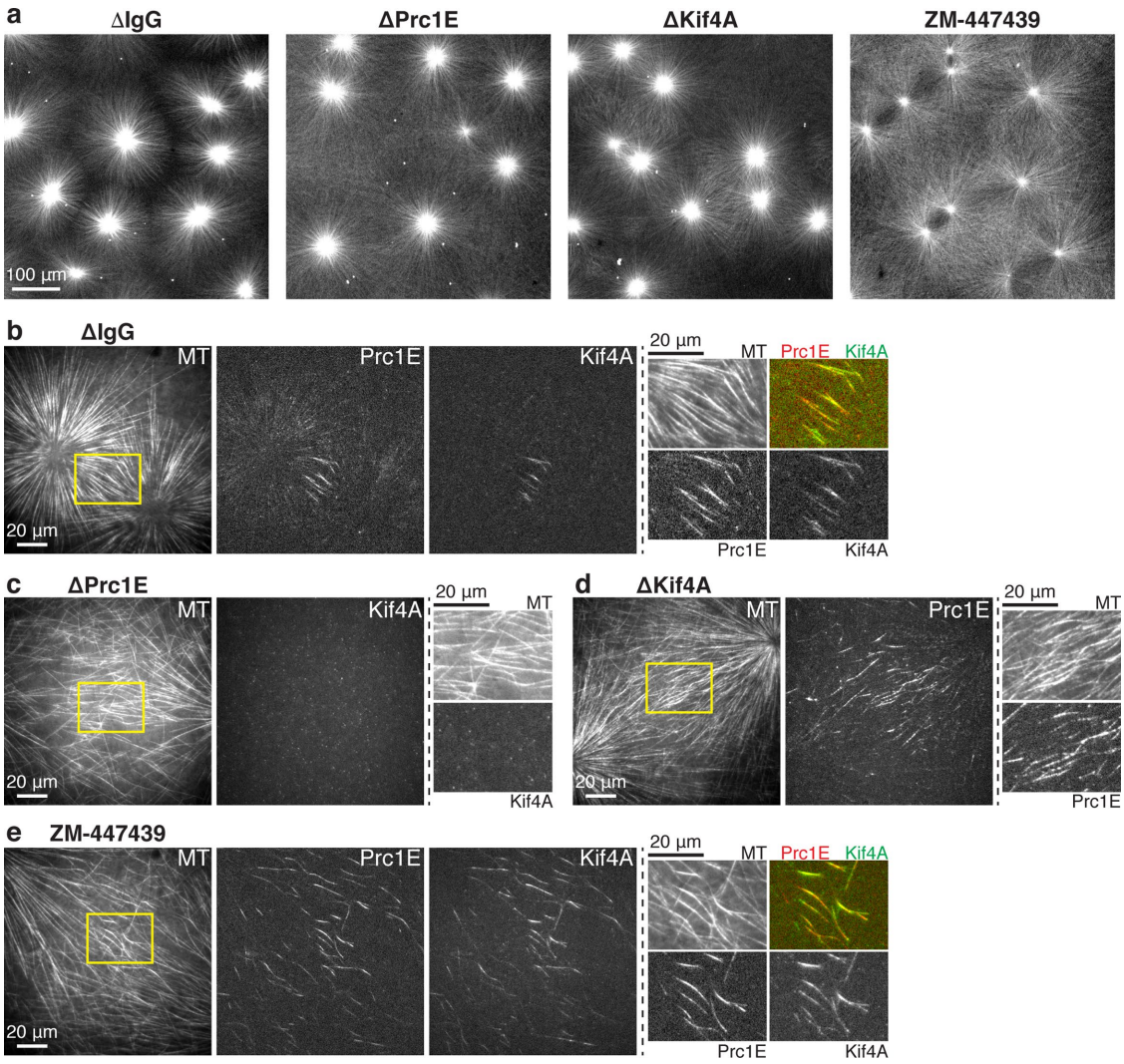

FIGURE 4: Immunodepletion of Prc1E and Kif4A. (a) Low-mag widefield tubulin images of asters depleted as shown or treated with 100 μM ZM-447439 (AurkB inhibitor). Prc1E and Kif4A depletion had no discernalbe effect on nucleation of microtubule density. AurkB inhibition caused descrease of MT density over time. (b–e) High-mag TIRF images showing microtubules (Alexa 647-tubulin), mCherry-Prc1E, and Kif4A-GFP under the depletion/inhibition above. Zoom-ups of boxed areas are shown on the right. Note that Kif4A localization to bundles depended on Prc1E. Prc1E localization did not depend on Kif4A, but bundles were more spread out in its absence. Both proteins were recruited to bundles when AurkB was inhibited, but the bundles are much more spread out.

Prc1E and Kif4A are required to block plus-end growth between asters

To quantify the effect of immunodepletion on microtubule growth between asters, we used EB1 comet tracking. The top panels in Figure 5a show tracking data and the bottom panels quantification of those data. The effects of depletions and add-backs are quantified as a bar graph in Figure 5g, where we report the distance over which EB1 directionality switches, using the arbitrary distance metric D60, the distance over which EB1 comet directionality switches from 60%: 40–40%:60%. For comparison, Figure 5g includes the effects of small molecule inhibition (ZM-447439) of the AurkB subunit of the CPC, which we previously showed increases D60 (Nguyen *et al.*, 2014).

Depletion of either Prc1E or Kif4A caused microtubules from each aster to grow into the neighboring aster much more than depletion using control IgG or anti-Kif23 (the kinesin subunit of Centralspindlin) (Figure 5, a–d). There was still a switch in microtubule orientation between the asters when Prc1E or Kif4A was depleted, but the distance over which this occurred was much larger. Thus, both proteins are required for a tightly organized block to microtubule interpenetration at the boundary between asters. EB1 comet visualization was superior using TIRF imaging of plus ends tracking along the surface of partially passivated coverslips. Supplemental Videos 4–6 show EB1 and tubulin between asters in control, Prc1E-depleted and Kif4A-depleted extracts. The block to plus-end growth between asters in control extracts, and loss of this block after depleting either protein, are clearly visualized.

The Prc1E depletion phenotype was rescued by adding back the appropriate recombinant expressed proteins, either as a GFP fusion or unlabelled protein (Figure 5e). Kif4A add back also rescued (unpublished data). This confirms both the specificity of the immunodepletion and the functional attributes of the recombinant proteins. The effect of Prc1E depletion was also rescued by adding back the somatic isoform of *Xenopus* Prc1 protein (Figure 5f). In

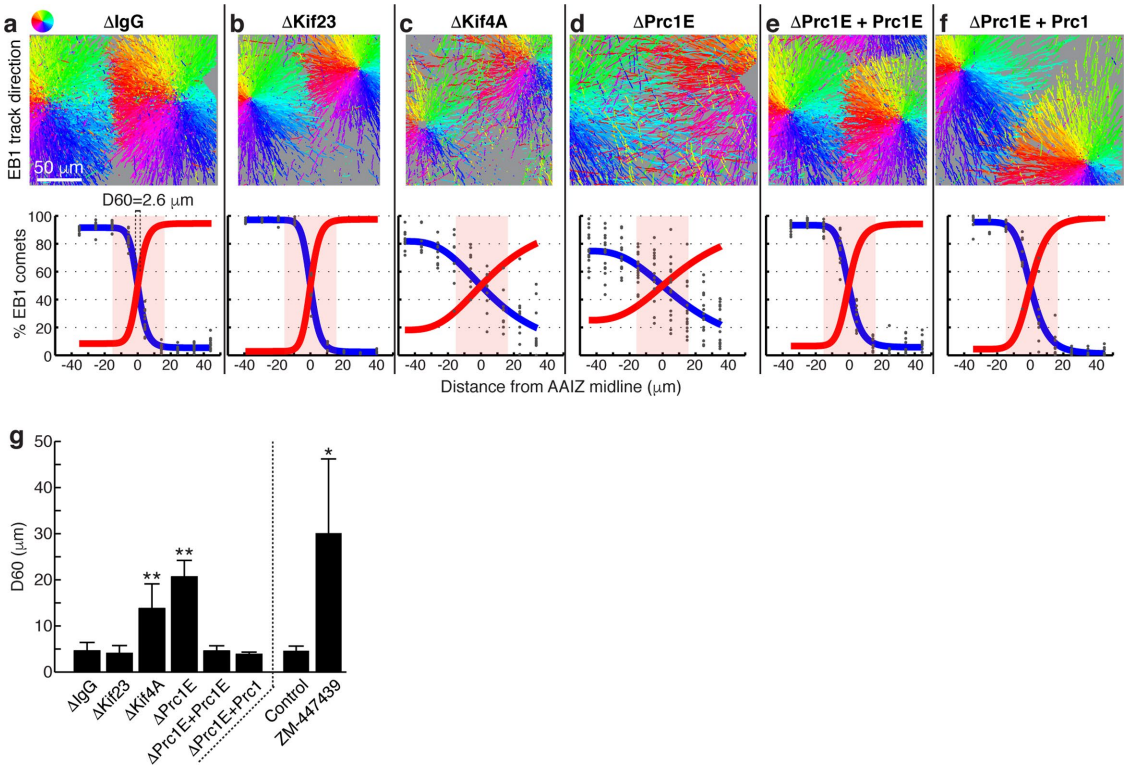

FIGURE 5: Prc1E and Kif4A are required for the block to interpenetration between asters. (a–f) Analyses of microtubule growth directions by EB1 tracking of spinning disk confocal images sequences as per Figure 2a. Depletions and add-backs as noted. (g) The D60 parameter, a metric for the degree of interpenetration, was defined as the difference between the interpolated distances where the red and blue curves crossed 60% (see panel a). Plot of mean D60 values (± SD) measured for each treatment ($n \geq 3$ interaction zones each). The last two bars (control and AurkB inhibition with 100 μM ZM-447439) were replotted from Nguyen *et al.* (2014) to provide a comparison. Asterisks indicate significant of different from control IgG depletion based on unpaired *t* test analyses, *$p < 0.01$, **$p < 0.001$.

general, we were unable to determine a functional difference between somatic and egg isoforms of Prc1 using the extract system.

The Prc1/Kif4A module enforces radial order within large asters

In the course of measuring the effects of Prc1E and Kif4A depletion on interaction zones between asters, we noticed that the morphology of isolated asters was also strongly perturbed. In control IgG-depleted extracts containing fewer nucleating beads, isolated asters grew with high radial order to the edge of the camera field (Figure 6a). In extracts depleted of either Prc1E or Kif4A, microtubules grew radially from the AurkA bead out to a radius of ~40 μm. Microtubules continued to assemble at the periphery, but instead of forming a well-organized aster, they appeared disorganized at larger radii. This effect is evident by the disorganized EB1 tracks at the periphery in Figure 6, b and c.

To quantify radial order in asters, we measured the directions of EB1 comet trajectories within a quadrant of an isolated aster with its center at the top left corner (Figure 6, a–e). We then generated radial order heat maps by plotting radial order parameters (*R*) calculated from the distribution of angular deviations of EB1 trajectories from the radial direction (Figure 6, a′–e′; see *Materials and Methods*). We also plotted average radial order parameters against the distance from the aster center at the AurkA bead (Figure 6f; see *Materials and Methods*). Radial order may be inaccurately measured at small radii (<10 μm) due to growth of microtubules in the *Z* plane close to the bead, so these plots were truncated at radii of less than 20 μm.

Mock depleted asters maintained high radial order out to the largest radius measured with our camera (~150–200 μm), with a slight decrease at large radii. Depletion of Kif4A or Prc1E strongly disrupted radial order. Limited order was maintained within ~40 μm radius, presumably due to frequent renucleation from the AurkA bead. Radial order was progressively lost as radius increased, though growth direction never completely randomized. The effect of depleting both Prc1E and Kif4A on radial order was rescued by adding back appropriate recombinant proteins (Figure 6, d and e; data not shown for Kif4A add-back). Both the embryonic and somatic isoforms of Prc1 were able to rescue radial order. We conclude from these data that Kif4A and Prc1E are necessary to maintain radial order within large asters as they expand, presumably to counter directional randomizing effects of nucleation away from the centrosome. Loss of radial order probably caused the gross disorganization of microtubules between asters we observed in Nguyen *et al.* (2014) when Kif4A was depleted and could not account for in that paper.

Pruning of anti-parallel microtubule overlaps by Prc1E and Kif4A

We finally turned to single microtubule imaging to better understand the function of Prec1E and Kif4A in asters. We sought regions in two- or three-color confocal movies where the microtubule density was low enough to image individual microtubules and then analyzed them by visual inspection and kymographs. Finding regions that were interpretable at the single microtubule level was

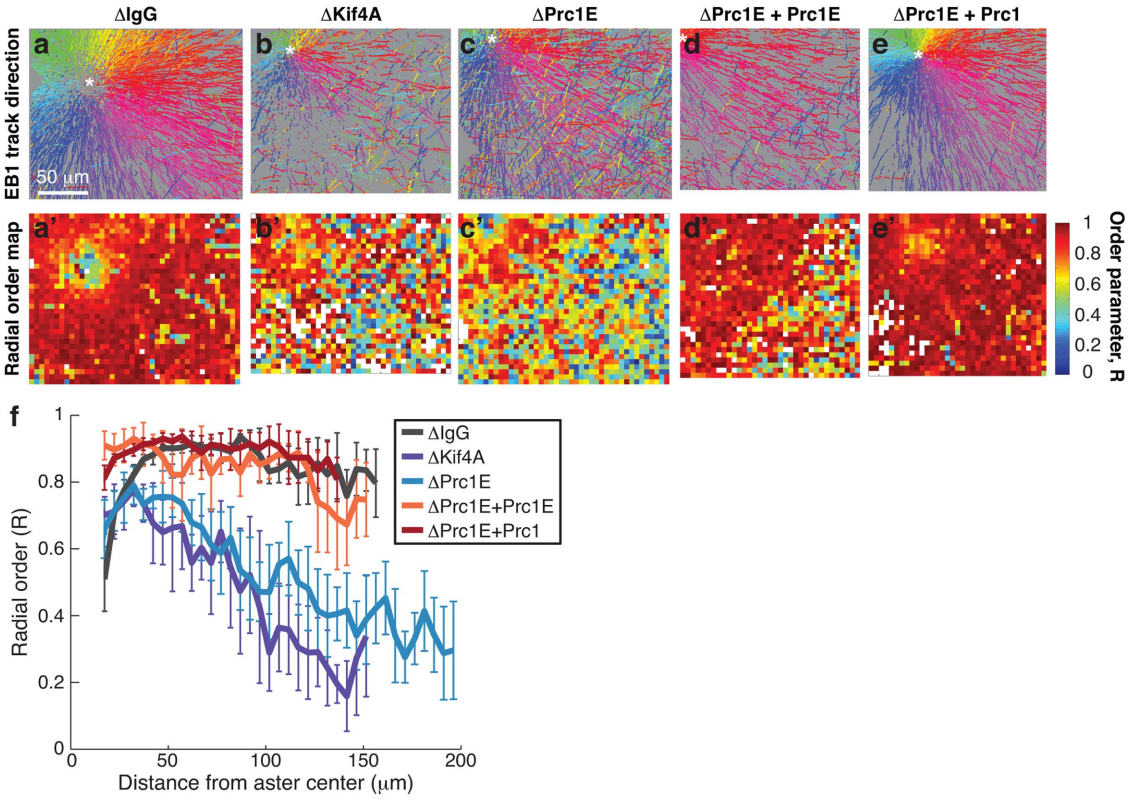

FIGURE 6: Prc1E and Kif4A enforce radial order in isolated asters. (a–e) Plus-end growth trajectories within isolated asters colored by mean direction. Imaging and EB1 tracking methods similar to Figure 2a. Asterisks indicate position of the nucleating center, Immunodepletion/add back conditions as labeled. (a′–e′) Radial order heat maps showing the local radial order quantified by the *R* parameter; each square cell measures 5 × 5 μm^2 (see *Materials and Methods*). Redder colors represent higher radial order. White pixels contained too few comet tracks to measure radial order. (f) Radial order parameter *R* as a function of distance from the aster center for the five asters shown above. Error bars are standard deviations (see *Materials and Methods* for analysis). Data are truncated at <20 μm, where microtubule growth components in the *z*-axis complicate analysis.

difficult because microtubule density was high, and most microtubules occurred in bundles of more than two. Figure 7 shows two examples near the edge of growing asters where a microtubule growing in the wrong direction enters an anti-parallel overlap, and then the overlap recruits Kif4A. In Figure 7a (Supplemental Video 7) a single microtubule growing in the wrong direction is evident in the first frame. It then enters an anti-parallel bundle that first recruits Kif4A and then shrinks. In Figure 7b (Supplemental Video 8) the incorrect microtubule may nucleate within in a bundle, which we suspect is more common. The bundle recruits Prc1E and Kif4A, and then proceeds to shrink, with loss of microtubule density. These movies support an anti-parallel pruning model for Prc1E/Kif4A function in asters, though we were not able to find enough clear examples to make any statistically justified statements concerning single microtubule mechanism.

DISCUSSION

Our data confirm much of what is already known about Prc1 and Kif4A function from published work from our laboratory and many others, for example, the localization of both factors to anti-parallel bundles prior to cytokinesis (Figures 1 and 2), a Prc1E requirement for recruitment of Kif4A to anti-parallel bundles (Figure 4), a role for protein in both organizing anti-parallel bundles (Figures 4 and 5) and restricting plus-end growth in anti-parallel bundles (Figure 5). In some cases, these confirmatory findings come with greatly improved quantification compared with previous work or/and extend work from somatic cells to the *Xenopus* egg system with its huge spatial scale, for example, precise quantification of plus-end dynamics between asters (Figure 3) and showing that Prc1E and Kif4A keep asters distinct in frog eggs by inhibiting plus-end growth at shared boundaries (Figure 5). Data in this paper also reveal new mechanisms and allow us to build new hypothesis, for example, evidence for depolymerization as well as stabilization in anti-parallel bundles (Figure 3i) and an unexpected role of the two proteins in enforcing radial order in isolated asters (Figure 6).

In Figure 8 we propose an "anti-parallel pruning" model to account for the role of Prc1E and Kif4 in generating the boundary between asters and enforcing radial order within them. This model combines Bieling and Surrey's molecular model from seminal biochemical reconstitution (Bieling *et al.*, 2010) with new information from the egg extract system. We propose that after Prc1E and Kif4 recognize anti-parallel bundles and slow plus-end growth, the plus ends eventually undergo catastrophe, so at least one of the anti-parallel microtubules is removed. We were not able to image catastrophes and depolymerization directly, except in occasional movies (Figure 7). It must nevertheless occur on the majority of microtubules that join anti-parallel bundles in the interaction zone because new plus ends continually enter anti-parallel bundles, yet total microtubule density remains approximately constant for many minutes (Figure 3i and Supplemental Video 4). Catastrophes were

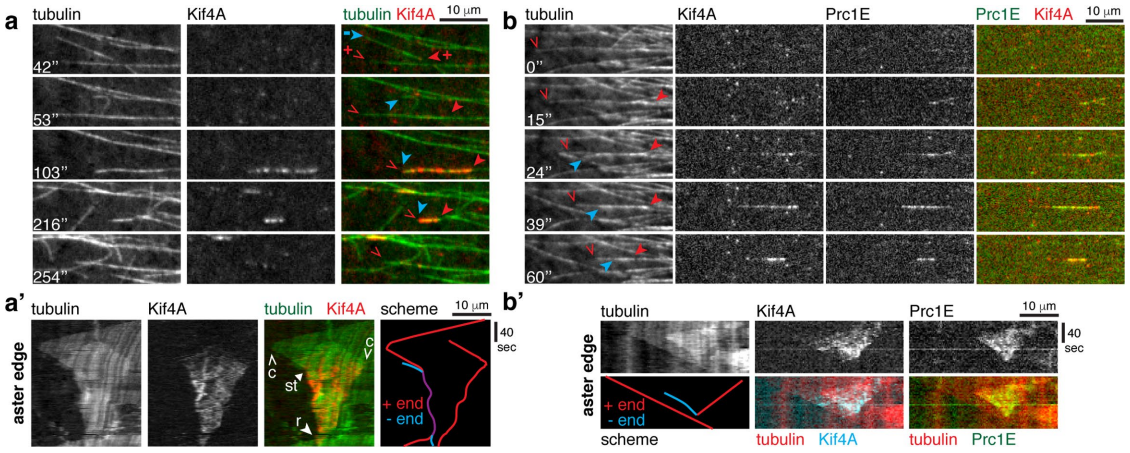

FIGURE 7: Examples of anti-parallel overlaps in growing asters being eliminated. Examples of anti-parallel microtubule overlap formation and elimination at the edge of growing asters imaged by spinning disk confocal microscopy (Supplemental Videos 7 and 8). Proteins visualized: (a) Alexa 647-tubulin and Kif4A-GFP, Alexa 647-tubulin; (b) Kif4A-GFP, and mCherry-Prc1E. Arrowheads indicate the following: likely plus ends (red), likely minus ends (cyan), microtubule growing out radially from aster (empty), and microtubule growing in opposite direction (full). (a',b') Kymographs of examples above along the radially growing microtubule. Events indicated: likely catastrophe (c), likely stabilization (st), and likely rescue (r).

not observed on plus ends coated with Prc1+Kif4A in pure protein systems (Bieling *et al.*, 2010; Subramanian *et al* 2013). We suspect that this was due to lack of catastrophe factors, though we note that pure protein work used PIPES buffer, pH 6.8, which is known to artificially stabilize microtubules and might also supress catastrophes. Higher pH is required to observe the catastrophe-promoting activity of stathmin, a different factor that negatively regulates plus-end dynamics (Howell *et al.*,1999).

Our model assumes that Prc1E and Kif4A transiently function together in anti-parallel overlaps, even though they do not strongly colocalize on average (Figure 2). Consistent with this assumption, we were able to observe examples of transient colocalization preceding anti-parallel pruning (Figure 7). Our model neglects other functions of both proteins. For example, Prc1E may contribute to the bundling of microtubules we observe throughout asters and may also help recruit CPC and centralspindlin to a subset of microtubules, as seen in somatic cells (Shrestha *et al.*, 2012).

Our model for the block to interpenetration between asters (Figure 8, red box) is essentially an extension of current ideas about somatic midzone organization applied to the much larger spatial scale of *Xenopus* zygotes, with the addition of a catastrophe step following recognition by Prc1E + Kif4A as discussed above. Our model for the role of Prc1E and Kif4A in enforcing radial order within asters (Figure 8, blue box) is a new idea and may be specific to very large egg cells. We propose radial order is enforced by the same anti-parallel pruning mechanism as the block to interpenetration between asters. Interphase asters must grow to radii of >500 μm to center the sperm pro-nucleus and orient the cleavage furrow in frog zygotes (Wühr *et al.*, 2010; Mitchison *et al.*, 2012). Radial order is presumably important to promote orderly aster growth and recruit cytokinesis signalling complexes selectively at the boundary between asters. Individual microtubules in the aster are short and unstable, with an estimated average length of ~16 μm (Ishihara *et al.*, 2016). We do not know the nucleation mechanism(s) of these microtubules.

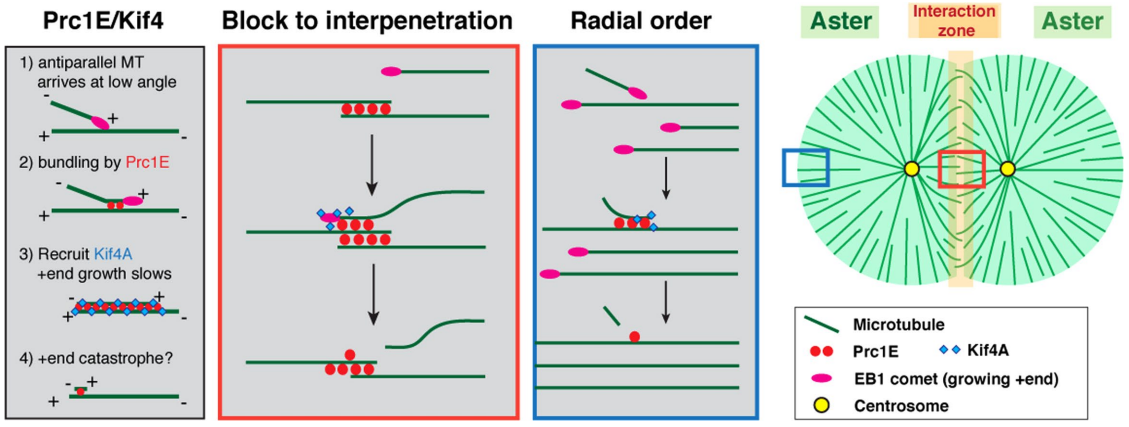

FIGURE 8: Model for function of Prc1E and Kif4A within and between asters. Left box, general function of Prc1E and Kif4A in anti-parallel bundles. Middle box, block to interpenetration at the interaction zone between asters. Right box, enforcement of radial order within single asters by pruning of anti-parallel overlaps. Left box, general function of Prc1E and Kif4A in anti-parallel bundles. Middle box, Block to interpenetration at the interaction zone between asters. Right box, enforcement of radial order within single asters by pruning of anti-parallel overlaps.

From imaging EB1 track initiations, we suspect nucleation occurs mostly within bundles (Ishihara *et al.*, 2014), and there is probably a preference for parallel nucleation, as observed in cytostatic factor (CSF)-arrested egg extracts (Petry *et al.*, 2013). However, the nucleation mechanisms likely differ, because TPX2 and Augmin, which play central roles in nucleating microtubules in meiosis-II spindles in CSF extract, did not seem to play a major role in interphase asters (Ishihara *et al.*, 2014). We observed ~3–10% of plus ends growing with the incorrect orientation in control asters (Figure 3, a and e), so we suspect that nucleation away from centrosomes can occur with incorrect orientation, at least in extracts, and that the anti-parallel pruning function of Prc1E and Kif4A removes these incorrectly orientated microtubules.

Activity of the AurkB subunit of the CPC was required for assembly of spatially focused interaction zones between asters (Figures 4e and 5g). However, AurkB activity was not required for recruitment of Prc1E and Kif4A to microtubule bundles inside asters (Figure 4e) or for growth of well-organized asters with correctly oriented plus ends (Nguyen *et al.*, 2014). We propose that the anti-parallel pruning function of Prc1E and Kif4A does not depend on AurkB activity, though the CPC helps focus it in CPC-positive interaction zones. When asters from different mitotic spindles, which we term "nonsister" asters, meet in polyspermic *Xenopus* zygotes, they fail to recruit CPC and centralspindlin to their shared boundary, and they also fail to trigger cleavage furrows (Field *et al.*, 2015). However, nonsister asters appeared not to cross into each other as they grew, and they formed distinct interaction zones at the shared boundary in microtubule images, albeit less focused than those between sister asters. We propose that Prc1E and Kif4A generate the boundary between nonsister asters in the same way they do between sisters, by anti-parallel pruning, though the boundary is less sharp in the absence of the spatial focusing activity of the CPC.

Many questions remain concerning the organization and dynamics of large interphase asters and the interaction zones that form between them. For example, we proposed that interaction zones constitute a bistable self-organizing system, which propagates outward with a memory of initial conditions, to explain how information on proximity to chromatin is propagated from the mitotic spindle to the cortex (Field *et al.*, 2015). The egg extract system will be useful to further address spatial communication from spindle to cortex, which was first characterized in detail by Rappaport in echinoderm eggs (Rappaport, 1996) and lies at the heart of the cleavage pattern of early embryos.

MATERIALS AND METHODS

Protein expression plasmid constructs

The *X. laevis* Prc1E coding sequence (codon optimized for *Escherichia coli* and insect cell expression; GenScript) was subcloned into pET-28b bacterial expression vector with an N-terminal Strep-tag (WSHPQFEK), creating Strep-Prc1E. To create the Strep-Prc1 construct, the Prc1E sequence was replaced with the *X. laevis* Prc1 somatic coding sequence from a published construct (Bieling *et al.*, 2010) kindly provided by Thomas Surrey (London Research Institute, UK). To create the Strep-mCherry-Prc1E construct, a mCherry coding sequence with a C-terminal AAA linker was inserted N-terminal to the Prc1E coding sequence. All subcloning was performed with Gibson cloning.

Proteins and antibodies

Xenopus laevis Kif4A-GFP-His was purified from Sf21 insect cells as described (Bieling *et al.*, 2010; Nguyen *et al.*, 2014). *Xenopus laevis* His-GFP-DasraA, human EB1-GFP-His, and human EB1-mCherry-His were purified from *E. coli* as described (Nguyen *et al.*, 2015). *Xenopus laevis* Strep-mCherry-Prc1E, Strep-Prc1E, and Strep-Prc1 were purified as previously described for a similar Strep-GFP-Prc1E construct (Nguyen *et al.*, 2014). Tubulin was purified from bovine brain and labeled with Alexa 488, Alexa 568, or Alexa 647 dyes (Life Technologies) as described (Hyman *et al.*, 1991). Protein concentrations were determined by Bradford assay with bovine serum albumin (BSA) standards and refer to dimers for tubulin and monomers for all the other proteins. See Supplemental Table S1 for sequence information on the *Xenopus* proteins studied in this paper.

Affinity-purified C-terminal peptide antibodies (rabbit) were produced against *X. laevis* Prc1E (C-FKEEMTKKSSHSEAVFNSTVNENL) (NeoBioLab). Antibodies were raised in rabbits to GST-fused *X. laevis* Prc1 (C-terminal 160 amino acids) and affinity purified using the Prc1 C-terminal tail fused to MBP. Affinity purified antibodies (rabbit) against C-terminal tails of *X. laevis* Kif4A, Kif23, and Aurora kinase B were from a previous study (Nguyen *et al.*, 2014). Tubulin antibodies (Sigma #T6074) were purchased. Antibodies were labeled on column with Alexa 488, Alexa 568, or Alexa 647 dyes (Life Technologies) as described (Groen *et al.*, 2014).

Passivation of glass coverslips

Fully passivated poly(ethylene glycol) (PEG)-coated coverslips were prepared either by following previous relatively labor-intensive protocols for covalently coating coverslips with silane-PEG (Bieling *et al.*, 2010) or by a much simpler coating with poly-(L-lysine)-PEG (PLL-PEG). For the latter method, coverslips were stored in 95% ethanol. On the day of use, they were withdrawn from the ethanol with forceps, flame dried in a Bunsen burner for a few seconds, and then cooled to room temperature (RT). They were incubated on one side with 100 µg/ml PLL-PEG {PLL(20)-g[3.5]-PEG(2), SuSoS, Switzerland} dissolved in 10 mM HEPES, pH 7.7, for 10–30 min at room temperature. Coverslips were rinsed several times in deionized water by transferring to drops on parafilm and then blow dried with nitrogen gas and used within 24 h. For TIRF imaging where we needed microtubules to track along the glass we used either coated with kappa casein or partial PEG passivation according to a published protocol (Portran, 2014). For these experiments, we made squashed between a fully passivated 22-mm^2 coverslip and a kappa casein coated, or partially passivated, 18-mm^2 coverslip (Portran, 2014) and imaged with less passivated coverslip.

Aster assembly assay

Metaphase-arrested *Xenopus* egg extracts with intact actin were prepared as described (Field *et al.*, 2014). Interphase asters were assembled between PEG-passivated coverslips as previously described (Nguyen *et al.*, 2014) with modifications in the coverslip passivation procedure described above. Briefly, M-phase extract was supplemented with fluorescent probes and treated with 0.4 mM $CaCl_2$ to mimic fertilization and induce metaphase-to-interphase transition. Activated extract was supplemented with Protein A Dynabeads (Life Technologies) coupled to Aurora kinase A antibody, which served as artificial centrosomes (Tsai and Zheng, 2005). Extract was then spread between two PEG-passivated glass coverslips. Aster assembly reactions were monitored with a widefield, spinning disk confocal, or a TIRF microscope at 20°C. For widefield and confocal imaging, asters were assembled between two fully passivated PEG-coated coverslips. For TIRF imaging, asters were assembled between a fully passivated PEG coverslip (top, 18 × 18 mm) and a partially passivated coverslip (bottom, 22 × 22 mm). Partial passivation allowed microtubules to track along the coated surface, within the TIRF illumination field. For visualization, fluorescent probes were

used at the following concentrations: 250 nM Alexa 488-, 568-, or 647-tubulin; 40 nM EB1-GFP or EB1-mCherry; 10 nM Kif4-GFP; 20 nM mCherry-Prc1E; and 20 nM GFP-DasraA.

Immunodepletions, protein addbacks, and drug inhibition

Prc1E, Kif4A, and Kif23 were depleted in two rounds using 2 × 20 µg of antibodies conjugated to 50 µl Protein A Dynabeads (Life Technologies) per 50 µl of extracts. Depletions using beads coated with random rabbit IgG served as controls. Depletions were confirmed by immunoblots. Kif4A depletion was rescued by adding back ~100 nM Kif4A-GFP, and Prc1E depletion was rescued by adding back ~65 nM purified Prc1E or Prc1. For inhibition of Aurora B kinase, 100 µM ZM447439 (Tocris Bioscience; 10 mM stock solution in 10 mM glycine, pH 7) was added to calcium activated extracts. Aster assembly assays were performed with treated extracts as described above.

All immunodepletion and drug inhibition experiments were performed with $n \geq 3$ biological repeats, using extracts prepared from eggs produced by different female frogs. Ideally, all the treatments ought to be performed on the same extract to reduce extract-to-extract (and frog-to-frog) variability, and the samples from each treatment ought to be imaged at the same time to reduce the variability introduced by the "aging" of extracts while stored on ice. In practice, however, this is impossible due to limitations posed by the amount of extract produced from a single female frog and our ability to handle samples. Therefore, we routinely performed only three to four treatments (including control buffer addition or IgG depletion) per experiment. Although we aimed to acquire data for all treatments simultaneously, one to two samples of the three to four would often be destroyed via mishandling, and thus the data for those treatments had to be acquired in the next round of aster assembly reaction.

Time-lapse fluorescence microscopy

Widefield images were obtained using a 10× Plan Apo 0.45 NA objective lens (Nikon) on an upright Nikon Eclipse 90i microscope equipped with a Prior Lumen 200 metal arc lamp, a Prior ProScan III motorized XY stage, a Hamamatsu ORCA-ER-cooled charge-coupled device (CCD) camera, and driven by Metamorph image acquisition software (Molecular Devices). Spinning disk confocal images were obtained using a 40× oil Plan Apo 1.30 NA objective lens (Nikon) on an upright Nikon Eclipse E800 microscope equipped with a Melles Griot Krypton/Argon ion laser (488, 568, 647 nm), a Yokogawa CSU-10 spinning disk (Perkin Elmer), a Hamamatsu ORCA-ER-cooled CCD camera, and driven by Metamorph. TIRF images were obtained using a 60× Apo TIRF 1.49 NA objective lens (Nikon) on a Nikon Ti-E motorized inverted microscope equipped with a Nikon motorized TIRF illuminator, Perfect focus, a Prior Proscan II motorized stage, Agilent MLC400B laser launch (488, 561, 647 nm), an Andor DU-897 EM-CCD camera driven by NIS-Elements image acquisition software. Two separate TIRF setups were available at the Nikon Imaging Center at Harvard Medical School and the Marine Biological Laboratory.

Fixed immunofluorescence of fixed *Xenopus* zygotes (Figure 1)

Zygotes were fixed and stained ~100 min after fertilization as previously described (Field *et al.*, 2015). Briefly, zygotes were fixed in a methanol/ethylene glycol-bis-(β-aminoethyl ether)-*N*,*N*,*N*′,*N*′-tetraacetic acid (EGTA) solution for 24 h at room temperature, rehydrated in a series of methanol/Tris-buffered saline mixtures, hemisected, bleached, and then incubated with directly labeled antibodies for at least 24 h at 4°C. Antibodies were used at approximately the following concentrations: Alexa 488-anti-tubulin (1–2 µg/ml), Alexa 568-anti-Prc1E (1–2 µg/ml), and Alexa 647-anti-Kif4A (1–2 µg/ml). Fixed zygotes were mounted in a mixture of benzyl alcohol and benzyl benzoate (Aldrich) and imaged with a laser scanning confocal microscope at the Nikon Imaging Center at Harvard Medical School. Imaging used a Nikon Ti-E inverted microscope with a Nikon A1R point scanning confocal head, driven by NIS-Elements image acquisition software.

Image analysis: microtubule plus-end dynamics from EB1 comet tracking (Figures 3, 5, and 6)

Time-lapse image sequences of EB1-GFP were acquired, processed, and analyzed as described (Nguyen *et al.*, 2014). Briefly, extract was supplemented with 40 nM EB1-GFP and 250 nM Alexa 647-tubulin. Asters were assembled between fully passivated PEG coverslips as described above. Lower AurkA bead density was used to study isolated asters and higher bead density to study interaction zones. Multiple isolated asters or interaction zones were imaged between 20 and 50 min of the assembly reaction at 20°C, alternating between control and treatment conditions. A spinning disk confocal microscope with a 40× oil objective (NA = 1.30) was used to acquire images with 2 × 2 binning. Time-lapse image sequences were acquired of EB1-GFP with 1.5-s intervals for a total duration of 2 min (81 frames total). Tubulin images were acquired at the beginning and end of each sequence.

EB1 image sequences were registered using the StackReg ImageJ plugin with rigid body transformation (Thévenaz *et al.*, 1998). The plusTipTracker MATLAB software (Applegate *et al.*, 2011) was used to perform automated detection and frame-to-frame linking of EB1 comets. Tracks were filtered out and excluded from analysis based on the criteria and parameters listed in Nguyen *et al.* (2014). Remaining tracks were then plotted and colored according to their mean direction (Figure 3a) or instantaneous velocity averaged over three consecutive frames (Figure 3b).

The degree of interpenetration was quantified by dividing all EB1 comets detected in frames 2–81 into two groups based on the direction of their displacement relative to the previous frame (Figure 3a′, inset showing "blue" and "red" directions). Rectangular regions of interests (ROIs; 90 µm × 10 µm) parallel to the bead-bead axis and traversing the interaction zone were overlaid. Each ROI was divided into 9 cells (10 µm × 10 µm each), and the fraction of EB1 comets moving in the "blue" direction was determined and plotted as gray dots against the distance from the interaction zone midline (see Figure S3 in Nguyen *et al.* (2014). The procedure was repeated for multiple nonoverlapping, neighboring ROIs within an interaction zone, giving rise to all the gray dot data. The data points were fitted to a sigmoidal distribution (Figure 3a′, blue curve):

$$f(x) = Y_{\min} + \frac{(Y_{\max} - Y_{\min})}{(1 + (a + x)^b)}$$

where x is distance and $f(x)$ is the fraction of EB1 comets moving in the "blue" direction. A complementary sigmoidal distribution described the fraction of EB1 comets moving in the other, "red," direction (Figure 3a′, red curve). The exact position of the interaction zone midline was defined where the blue and red curves intersected. A "D60" parameter was defined as the difference between the interpolated distances where the red and blue curves crossed 60%. This parameter served as a measure for the depth of interpenetration.

The instantaneous velocities associated with each EB1 comet detected in frames 2–81 were averaged within each square cell. The total number of EB1 comets was counted, and the comet density determined for each cell. The number of EB1 comets comprising

the initiation or the termination of a growth track was counted and expressed as the fraction of total EB1 comets for each cell. EB1 comet speeds, densities, track terminations, and initiations were averaged for cells in neighboring ROIs at a given distance from the interaction zone midline. These mean values were plotted in Figure 3, b′ and c′, where the error bars indicate SEMs for EB1 speeds and SDs for densities, track terminations, and initiations.

To obtain the percentage difference in plus-end dynamics measurements inside an interaction zone compared with outside, the mean value of each measurement obtained at the exact interaction zone midline (0 µm) was divided by the mean of the mean values obtained at –40, –30, –20, 20, 30, and 40 µm from the interaction zone midline. The mean values obtained at –10 and 10 µm were considered transition values and thus were omitted from the calculations. The percentage difference measurements were averaged for multiple ($n \geq 3$) interaction zones per condition; the mean values were plotted with standard deviations as error bars in Figure 4). All analyses were performed in MATLAB.

Image analysis: quantification of radial order within isolated asters

The first approach to quantifying radial order in asters involved tracking EB1 comets over 2 min (81 frames at 1.5-s intervals) and measuring their directions (angles of frame-to-frame displacement) within a quadrant of an isolated aster. Radial order heat maps were created by dividing the field of view into square cells measuring 5 × 5 µm^2 (Figure 6, a′–e′). A radial order parameter (*R*) was calculated from the distribution of angular deviations of EB1 comet directions from the radial direction within each square cell:

$$R = \frac{1}{N}\left|\sum_{n=1}^{N}\left(\cos(\theta_n) + i\sin(\theta_n)\right)\right| = \frac{1}{N}\left|\sum_{n=1}^{N} e^{-i\theta_n}\right|$$

where $\theta_n = \beta_n - \alpha_n$. The variable α_n is the radial direction of each EB1 comet (i.e., angular coordinate within a polar coordinate system with the aster center as the pole), and β_n is the angle of displacement of each comet with respect to the previous frame. The variable θ_n ranges from $-\pi$ to $+\pi$ in radians. For the heat maps, all EB1 comets detected from frame 2–81 were considered within each square cell. In directional statistics, the circular variance is defined as (*1 - R*), which is a measure of the spread of a population of angles θ_n. *R* is the length of the mean resultant vector of the population of angles and ranges from 0 to 1. A MATLAB toolbox called "CircStat" was used to compute the resultant vector length (*R*) (Berens, 2009). To quantify the dependence of radial order on the distance from the aster center, the field of view was divided into concentric rings with a width of 5 µm, centering on the AurkA bead. Radial order parameters (*R*) were obtained for each ring area, considering EB1 comets detected within 10 consecutive frames (e.g., frames 2–11, 12–21, …, 72–81). Figure 6f shows the average values of the *R* parameter as a function of aster radius for different conditions. Each *R* value was averaged across all eight time ranges in the image sequence. The error bars are the standard deviation of these *R* values from the mean and represent the fluctuation of the *R* value over time, combined with measurement error.

REFERENCES

Applegate KT, Besson S, Matov A, Bagonis MH, Jaqaman K, Danuser G (2011). plusTipTracker: quantitative image analysis software for the measurement of microtubule dynamics. J Struct Biol 176, 168–184.

Argiros H, Henson L, Holguin C, Foe V, Shuster CB (2012). Centralspindlin and chromosomal passenger complex behavior during normal and Rappaport furrow specification in echinoderm embryos. Cytoskeleton (Hoboken) 69, 840–853.

Basant A, Lekomtsev S, Tse YC, Zhang D, Longhini KM, Petronczki M, Glotzer M (2015). Aurora B kinase promotes cytokinesis by inducing centralspindlin oligomers that associate with the plasma membrane. Dev Cell 33, 204–215.

Berens P (2009). Circstat: a MATLAB toolbox for circular statistics. J Stat Softw 31, 1–21.

Bieling P, Telley IA, Surrey T (2010). A minimal midzone protein module controls formation and length of antiparallel microtubule overlaps. Cell 142, 420–432.

Bringmann H, Skiniotis G, Spilker A, Kandels-Lewis S, Vernos I, Surrey T (2004). A kinesin-like motor inhibits microtubule dynamic instability. Science 303, 1519–1522.

Canman JC, Cameron LA, Maddox PS, Straight A, Tirnauer JS, Mitchison TJ, Fang G, Kapoor TM, Salmon ED (2003). Determining the position of the cell division plane. Nature 424, 1074–1078.

Canman JC, Lewellyn L, Laband K, Smerdon SJ, Desai A, Bowerman B, Oegema K (2008). Inhibition of Rac by the GAP activity of centralspindlin is essential for cytokinesis. Science 322, 1543–1546.

Field CM, Groen AC, Nguyen PA, Mitchison TJ (2015). Spindle-to-cortex communication in cleaving, polyspermic Xenopus eggs. Mol Biol Cell 26, 3628–3640.

Field CM, Nguyen PA, Ishihara K, Groen AC, Mitchison TJ (2014). Xenopus egg cytoplasm with intact actin. Methods Enzymol 540, 399–415.

Field CM, Pelletier JF, Mitchison TJ (2017). Xenopus extract approaches to studying microtubule organization and signaling in cytokinesis. Methods Cell Biol 137, 395–435.

Glotzer M (2009). The 3Ms of central spindle assembly: microtubules, motors and MAPs. Nat Rev Mol Cell Biol 10, 9–20.

Groen AC, Ngyuen PA, Field CM, Ishihara K, Mitchison TJ (2014). Glycogen-supplemented mitotic cytosol for analyzing Xenopus egg microtubule organization. Methods Enzymol 540, 417–433.

Gruneberg U, Neef R, Honda R, Nigg EA, Barr FA (2004). Relocation of Aurora B from centromeres to the central spindle at the metaphase to anaphase transition requires MKlp2. J Cell Biol 166, 167–172.

Henson JH, Buckley MW, Yeterian M, Weeks RM, Simerly CR, Shuster CB (2016). Central spindle self-organization and cytokinesis in artificially activated sea urchin eggs. Biol Bull 230, 85–95.

Howell B, Larsson N, Gullberg M, Cassimeris L (1999). Dissociation of the tubulin-sequestering and microtubule catastrophe-promoting activities of oncoprotein 18/stathmin. Mol Biol Cell 10, 105–118.

Hu C-K, Coughlin M, Field CM, Mitchison TJ (2008). Cell polarization during monopolar cytokinesis. J Cell Biol 181, 195–202.

Hu C-K, Coughlin M, Field CM, Mitchison TJ (2011). KIF4 regulates midzone length during cytokinesis. Curr Biol 21, 815–824.

Hyman A, Drechsel D, Kellogg D, Salser S, Sawin K, Steffen P, Wordeman L, Mitchison T (1991). Preparation of modified tubulins. Methods Enzymol 196, 478–485.

Ishihara K, Korolev KS, Mitchison TJ (2016). Physical basis of large microtubule aster growth. Elife 5, e19145.

Ishihara K, Nguyen PA, Groen AC, Field CM, Mitchison TJ (2014). Microtubule nucleation remote from centrosomes may explain how asters span large cells. Proc Natl Acad Sci USA 111, 17715–17722.

Jantsch-Plunger V, Gönczy P, Romano A, Schnabel H, Hamill D, Schnabel R, Hyman AA, Glotzer M (2000). CYK-4: A Rho family gtpase activating protein (GAP) required for central spindle formation and cytokinesis. J Cell Biol 149, 1391–1404.

Jiang W, Jimenez G, Wells NJ, Hope TJ, Wahl GM, Hunter T, Fukunaga R (1998). PRC1: a human mitotic spindle-associated CDK substrate protein required for cytokinesis. Mol Cell 2, 877–885.

Kurasawa Y, Earnshaw WC, Mochizuki Y, Dohmae N, Todokoro K (2004). Essential roles of KIF4 and its binding partner PRC1 in organized central spindle midzone formation. EMBO J 23, 3237–3248.

Lewellyn L, Carvalho A, Desai A, Maddox AS, Oegema K (2011). The chromosomal passenger complex and centralspindlin independently contribute to contractile ring assembly. J Cell Biol 193, 155–169.

Mastronarde DN, McDonald KL, Ding R, McIntosh JR (1993). Interpolar spindle microtubules in PTK cells. J Cell Biol 123, 1475–1489.

McIntosh JR, Euteneuer U (1984). Tubulin hooks as probes for microtubule polarity: an analysis of the method and an evaluation of data on microtubule polarity in the mitotic spindle. J Cell Biol 98, 525–533.

Mishima M, Kaitna S, Glotzer M (2002). Central spindle assembly and cytokinesis require a kinesin-like protein/RhoGAP complex with microtubule bundling activity. Dev Cell 2, 41–54.

Mitchison T, Wühr M, Nguyen P, Ishihara K, Groen A, Field CM (2012). Growth, interaction, and positioning of microtubule asters in extremely large vertebrate embryo cells. Cytoskeleton (Hoboken) 69, 738–750.
Mitchison TJ, Nguyen P, Coughlin M, Groen AC (2013). Self-organization of stabilized microtubules by both spindle and midzone mechanisms in Xenopus egg cytosol. Mol Biol Cell 24, 1559–1573.
Mollinari C, Kleman J-P, Jiang W, Schoehn G, Hunter T, Margolis RL (2002). PRC1 is a microtubule binding and bundling protein essential to maintain the mitotic spindle midzone. J Cell Biol 157, 1175–1186.
Nguyen PA, Field CM, Groen AC, Mitchison TJ, Loose M (2015). Using supported bilayers to study the spatiotemporal organization of membrane-bound proteins. Methods Cell Biol 128, 223–241.
Nguyen PA, Groen AC, Loose M, Ishihara K, Wühr M, Field CM, Mitchison TJ (2014). Spatial organization of cytokinesis signaling reconstituted in a cell-free system. Science 346, 244–247.
Peshkin L, Wühr M, Pearl E, Haas W, Freeman RM, Gerhart JC, Klein AM, Horb M, Gygi SP, Kirschner MW (2015). On the relationship of protein and mRNA dynamics in vertebrate embryonic development. Dev Cell 35, 383–394.
Petry S, Groen AC, Ishihara K, Mitchison TJ, Vale RD (2013). Branching microtubule nucleation in Xenopus egg extracts mediated by augmin and TPX2. Cell 152, 768–777.
Portran D (2014). Micropatterning microtubules. Methods Cell Biol 120, 39–51.
Rappaport R (1996). Cytokinesis in animal cells (Cambridge University Press).
Rodrigues NTL, Lekomtsev S, Jananji S, Kriston-Vizi J, Hickson GRX, Baum B (2015). Kinetochore-localized PP1-Sds22 couples chromosome segregation to polar relaxation. Nature 524, 489–492.
Saxton WM, McIntosh JR (1987). Interzone microtubule behavior in late anaphase and telophase spindles. J Cell Biol 105, 875–886.
Shrestha S, Wilmeth LJ, Eyer J, Shuster CB (2012). PRC1 controls spindle polarization and recruitment of cytokinetic factors during monopolar cytokinesis. Mol Biol Cell 23, 1196–1207.
Subramanian R, Ti S-C, Tan L, Darst SA, Kapoor TM (2013). Marking and measuring single microtubules by PRC1 and kinesin-4. Cell 154, 377–390.
Subramanian R, Wilson-Kubalek EM, Arthur CP, Bick MJ, Campbell EA, Darst SA, Milligan RA, Kapoor TM (2010). Insights into antiparallel microtubule crosslinking by PRC1, a conserved nonmotor microtubule binding protein. Cell 142, 433–443.
Thévenaz P, Ruttimann UE, Unser M (1998). A pyramid approach to subpixel registration based on intensity. IEEE Trans Image Process 7, 27–41.
Tsai M-Y, Zheng Y (2005). Aurora A kinase-coated beads function as microtubule-organizing centers and enhance RanGTP-induced spindle assembly. Curr Biol 15, 2156–2163.
Vernos I, Raats J, Hirano T, Heasman J, Karsenti E, Wylie C (1995). Xklp1, a chromosomal Xenopus kinesin-like protein essential for spindle organization and chromosome positioning. Cell 81, 117–127.
White JG, Borisy GG (1983). On the mechanisms of cytokinesis in animal cells. J Theor Biol 101, 289–316.
Wühr M, Freeman RM, Presler M, Horb ME, Peshkin L, Gygi SP, Kirschner MW (2014). Deep proteomics of the Xenopus laevis egg using an mRNA-derived reference database. Curr Biol 24, 1467–1475.
Wühr M, Tan ES, Parker SK, Detrich HW 3rd, Mitchison TJ (2010). A model for cleavage plane determination in early amphibian and fish embryos. Curr Biol 20, 2040–2045.
Yüce O, Piekny A, Glotzer M (2005). An ECT2-centralspindlin complex regulates the localization and function of RhoA. J Cell Biol 170, 571–582.
Zhu C, Jiang W (2005). Cell cycle-dependent translocation of PRC1 on the spindle by Kif4 is essential for midzone formation and cytokinesis. ProcNatl Acad Sci USA 102, 343–348.